INTERNATIONAL JOURNAL OF
RADIATION ONCOLOGY • BIOLOGY • PHYSICS
www.redjournal.org

PHYSICS CONTRIBUTION

FLASH Bragg-Peak Irradiation With a Therapeutic Carbon Ion Beam: First In Vivo Results

Walter Tinganelli, PhD,[*] Anggraeini Puspitasari-Kokko, MD, PhD,[†] Olga Sokol, PhD,[*] Alexander Helm, PhD,[*] Palma Simoniello, PhD,[‡] Christoph Schuy, PhD,[*] Sylvie Lerchl, PhD,[*] Denise Eckert, PhD,[*] Julius Oppermann, MSc,[*] Anna Rehm, PhD,[§] Stefan Janssen, PhD,[§] Denise Engel, PhD,[‖] Ralf Moeller, PhD,[‖,§§] Rossana Romano, MSc,[‡] Felix Horst, PhD,[¶,#] Daria Boscolo, PhD,[*] Claudia Fournier, PhD,[*] Marco Durante, PhD,[*,**,††] and Uli Weber, PhD[*,‡‡]

[*]*GSI Helmholtzzentrum für Schwerionenforschung, Biophysics Department, Darmstadt, Germany;* [†]*Department of Research and Development, Holland PTC, Delft, The Netherlands;* [‡]*Department of Science and Technology, University of Naples Parthenope, Naples, Italy;* [§]*Algorithmic Bioinformatics, Justus Liebig University, Giessen, Germany;* [‖]*German Aerospace Center, Institute of Aerospace Medicine, Radiation Biology Department, Aerospace Microbiology, Cologne/Köln, Germany;* [¶]*OncoRay – National Center for Radiation Research in Oncology, Faculty of Medicine, Dresden, Germany;* [#]*Helmholtz-Zentrum Dresden-Rossendorf, Institute of Radiooncology – OncoRay, Dresden, Germany;* [**]*Department of Physics, Institute of Condensed Matter Physics, Technische Universität Darmstadt, Darmstadt, Germany;* [††]*Department of Physics "Ettore Pancini," University Federico II, Naples, Italy; and* [‡‡]*Life Science Engineering Department, Technische Hochschule Mittelhessen, Gießen, Germany*

Received May 6, 2024; Accepted for publication Nov 10, 2024

Purpose: In recent years, ultra-high dose rate (UHDR) irradiation has emerged as a promising innovative approach to cancer treatment. Characteristic feature of this regimen, commonly referred to as FLASH effect, demonstrated primarily for electrons, photons, or protons, is the improved normal tissue sparing, whereas the tumor control is similar to the one of the conventional dose-rate (CDR) treatments. The FLASH mechanism is, however, unknown. One major question is whether this effect is maintained when using densely ionizing (high-LET) heavy nuclei.

Methods Materials: Here, we report the effects of 20 Gy UHDR heavy ion irradiation in clinically relevant conditions, ie, at high-LET in the spread-out Bragg peak of a ^{12}C beam using an osteosarcoma mouse model.

Results: We show that UHDR irradiation was less toxic in the normal tissue compared with CDR while maintaining tumor control. The immune activation was also comparable in UHDR and CDR groups. Both UHDR and CDR exposures steered the metagenome toward a balanced state.

Conclusions: These results suggest that the UHDR irradiations can improve the safety and effectiveness of heavy ion therapy, and provide a crucial benchmark for current mechanistic FLASH models. However, additional experiments are needed to validate these findings across other animal and tumor models.

Corresponding author: Marco Durante, PhD; E-mail: m.durante@gsi.de

Disclosures: none. This work was funded by the European Union's Horizon Europe research and Innovation programme under Grant Agreement No. 101057511 (EURO-LABS).

[§§]Deceased

Supplementary material associated with this article can be found in the online version at doi:10.1016/j.ijrobp.2024.11.089.

Int J Radiation Oncol Biol Phys, Vol. 121, No. 5, pp. 1282–1292, 2025
0360-3016/$ - see front matter
https://doi.org/10.1016/j.ijrobp.2024.11.089

Introduction

Ultra-high dose rate (UHDR) irradiation has the potential to widen the therapeutic window by reducing the damage to healthy tissues while maintaining the tumor control (commonly referred to as the FLASH effect), as compared with the treatments at conventional dose rates (CDR).[1,2]

The protective effect of FLASH relies not only on the dose rate but also on total dose, spill structure, and biological endpoint.[1,3,4] Several hypotheses proposed to explain the mechanism of the FLASH effect.[5] Most models are based on radiation chemistry. The FLASH effect might stem from the rapid generation of free radicals and distinctions in redox and free radical chemistry between normal and tumor tissues, resulting in significantly higher energy deposition and ionization events for a given isodose in UHDR mode compared with CDR mode.[6] Another hypothesis suggests that irradiation at UHDR might partially deplete oxygen in the tissues, causing temporal hypoxia an thus increasing their radioresistance.[7] Moreover, biological factors might be at play, such as changes in the immune system response to radiation or altered signaling pathways within cells exposed to UHDR.[8,9] UHDR may also differently affect the tumor blood vessels (ie, causing less damage), potentially preventing changes in tumor vasculature that could affect its response to treatment (eg, through better immune cells infiltration).[10] Interestingly, all models predicts that the FLASH effect should be linear energy transfer (LET)-dependent, with a tendency to disappear at high-LET.[11] Experiments with heavy ions in FLASH conditions are therefore interesting for 3 reasons: (1) test of the current mechanistic models at high-LET;[11] (2) clinical implementation in C-ion therapy[12]; and (3) if the sparing effect survives at high-LET, possibility of using very heavy ions (such as ^{20}Ne or ^{40}Ar) in therapy, and idea originally pursued by Cornelius Tobias at the Lawrence Berkeley Laboratory.[13,14]

We have recently shown the feasibility of UHDR irradiations with carbon ion beams and confirmed the FLASH effect in vitro and in vivo with heavy ions.[15,16] However, those experiments were performed in the plateau region of ^{12}C-ion Bragg curve with relatively low-LET values (<20 keV/μm). In heavy ion therapy, tumors are exposed in the Bragg-peak region, which has to be widened to cover the whole tumor volume (spread-out Bragg peak [SOBP]). In the SOBP, the beam LET is substantially higher (typically 40-80 keV/μm) resulting in an increased biological effectiveness,[17] especially for hypoxic tumors.[18]

Here, we present the first results of normal and tumor tissue irradiation in the SOBP (20 Gy, LET ≈65-85 keV/μm) of ^{12}C ions at ultra-high (>100 Gy/s) dose rates accelerated at SIS18 synchrotron of the GSI Helmholyz Center. Our goal was to investigate whether FLASH irradiation at the Bragg peak induces distinct biological effects, taking into account our previous findings with low-LET carbon ion irradiation.[16] The biological model was the LM8 osteosarcoma injected in the hind limb of C3H/He mice.

We demonstrated the FLASH effect in relation to tumor growth and normal muscle tissue damage. Additionally, we investigated the impact of UHDR irradiation with high-LET ions on metastasis formation, both local and systemic immune responses, as well as alterations in the gut microbiome.

Methods and Materials

Animal model

All experiments were performed using 4-week-old female C3H/He mice (Charles River Laboratories) according to German federal law and with the approval of the Hessen Animal Ethics Committee (Project license DA17/2000). A total of 44 mice were used for the experiments. Mice were divided into 4 groups: UHDR (14 animals), CDR (15 animals), sham irradiated (10 animals), and no tumor (5 animals). The mice were housed at GSI in a conventional animal facility (non-SPF), at ∼22 °C and a 12-hour light-dark cycle. They were provided with unrestricted access to a standard diet (Ssniff) and water. Seven days before irradiation, mouse Dunn osteosarcoma LM8 cells (originating from C3H/He mice, purchased from Riken BioResource Center were injected subcutaneously in the right posterior limb of the mice (10^6 in 20 μL of DMEM medium with 10% fetal bovine serum and 1% Pen/Strep). After 1 week, the tumors were palpable and measurable.

Irradiation

Irradiations were performed in the Cave A branch of the SIS18 synchrotron at the GSI Helmholtz Center in Darmstadt, Germany. A beam of 240 MeV/u ^{12}C-ions was extracted in air. The beam line and setup were similar as shown and described in Tinganelli et al[16], whereas the general concept of the dosimetry system in the vault is described in Luoni et al.[19] However, for the UHDR irradiation some modifications were applied (see Supplementary materials, irradiation setup and dosimetry).

Mice were anesthetized with isoflurane and then irradiated (20 Gy) inside an airtight plastic box flushed with isoflurane at a specific rate to maintain anesthesia. Because the irradiation field, particularly the lateral dose fall-off, exceeded the target volume, we shielded the mice bodies with brass absorbers to prevent side effects in adjacent organs (Fig. 1A). The positions of the limbs were adjusted 10 mm before the distal edge of the SOBP using a plastic absorber of 60 mm water equivalent thickness. Because of the strong gradient, the dose-averaged LET in the target volume varied between 65 and 85 keV/μm (Fig. 1B).

The treatment field was applied by the Cave A raster scanning system with a scanning pattern of 21 × 21 mm^2 (8 × 8 beam spots, step size of 3 mm) and a pencil beam of ≈6mm full width half maximum, yielding a highly homogenous dose in the inner area of 15 × 15 mm^2.The SOBP with an

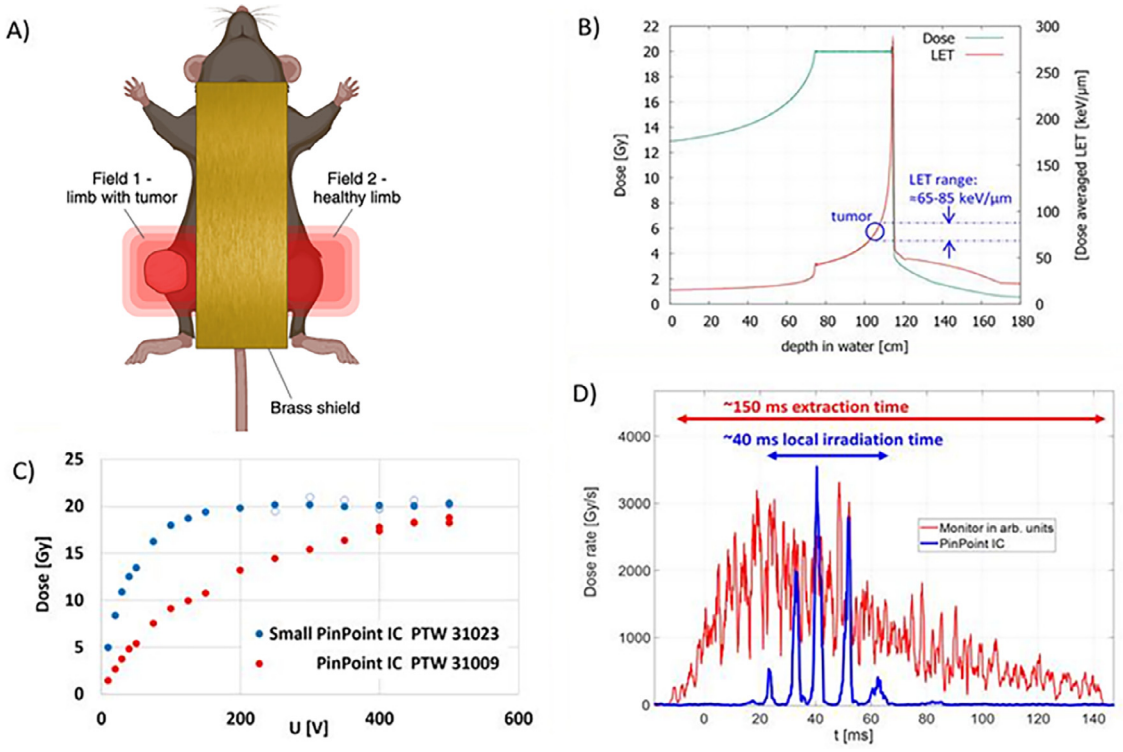

Fig. 1. Setup for the FLASH (UHDR) and CDR irradiation. (A) Mice irradiated successively with two 20 Gy fields (either CDR or UHDR, ≈15 × 15 mm^2 homogeneous area) for the tumor-bearing limb and the healthy limb. Adjacent organs were shielded by a 25 × 80 mm^2 and 10 mm thick block of brass. (B) Depth-dose and LET distribution from the 240 MeV/u ^{12}C beam modulated by the 2DRM into a 4-cm SOBP. Tumor depth is adjusted at 10 mm before distal edge by absorbers. (C) Saturation curves at UHDR conditions for 2 different PinPoint chambers, type 31023 chamber was selected for dosimetry. (D) Time-resolved signal and local dose rate (mid of target volume) from the beam monitor and the PinPoint IC (PTW 31023), respectively, showing the total and local irradiation time at the center of the target. *Abbreviations:* 2DRM = 2D range modulator; CDR = conventional dose rate; LET = linear energy transfer; SOBP = spread-out Bragg peak; UHDR = ultra-high dose rate.

extension of 4 cm was realized by a so-called 2D range modulator[19,20] with a pin period of 2 mm and a pin height of ca. 40 mm. It was placed in a distance of 50 cm from the target to avoid the edge scattering inhomogeneities from the modulator.[21] The modulator was precisely printed with a stereo lithography 3D-printer (3D-Systems). Additionally, a standard 3 mm ripple filter[22] was installed at the exit window to further smoothen the depth dose profile.

Tumor growth measurements

Tumor size was measured with a Vernier caliper approximately every second day for 24 days after irradiation. Mice were killed 35 days after tumor inoculation. Tumors had approximately hemiellipsoid shapes and therefore their volumes were calculated from the measured length (a), width (b), and depth (c) as $V = (\pi \times a \times b \times c) / 6$. Statistical analysis was done using a T-test between the different groups.

Histological analysis

Twenty-eight days after irradiation, animals were killed and the primary tumor, lungs, spleen, and both limbs were collected for further analysis. Limb muscles and tumors were fixed in 4% neutral buffered formalin for 24 hours. After 24 hours, the specimens were dehydrated in a Tissue Processor (Leica HistoCore Pegasus) according to the manufacturer settings, embedded in paraffin (Leica; HistoCore Arcadia Embedding Center) and sequentially cut and stained with hematoxylin (Gill No.3, Sigma-Aldrich) and 0.5% aqueous eosin solution (Carl Roth) according to the manufacturer protocol. To assess the level of fibrosis in limb muscles, Picrosirius Red staining according to refs.[23,24] was performed. Using a microtome (RM2235, Leica Microsystems), tumors were cut into 5 μm slices. To stain for CD8 alpha positive cells, tumor slices were processed with rabbit recombinant anti-CD8 alpha (monoclonal, ab209775, Abcam) as primary antibody as previously described.[24,25] Subsequently, a digitizer for slides (Axio Scan.Z1, Carl Zeiss Microscopy) was used to image 2-3 entire slices of each tumor (n = 5-11 tumors per treatment group). Further details are given in the Supplementary material.

Skin toxicity analysis

For the skin toxicity analysis, each animal was evaluated and assigned a damage score based on the observed severity of

skin changes. The scoring system was as follows: a score of 0 indicated no damage, a score of 1 denoted skin peeling and redness, and a score of 2 represented the presence of small wounds. This standardized scoring approach facilitated a consistent assessment of skin toxicity across all experimental groups.

Lung metastasis analysis

After the animals were killed, the bilateral lungs were collected and placed in Bouin solution (Sigma-Aldrich) for 24 hours. An operator with a stereoscope counted the metastatic nodules on the pulmonary surfaces. The average incidence of lung metastases was expressed as relative values compared with that of the control group.[25] Statistical analysis was performed via Mann-Whitney test using the GraphPad Prism 9 software.

Flow cytometry analysis

To obtain single cell suspensions of tumors, spleen, and lymph nodes, the isolated tumors or organs were manually disrupted using tissue strainers (40 or 100 μm; Greiner Bio-One). A subsequent lysis of red blood cells was performed for 5 minutes in a buffer containing ammonium chloride, potassium hydrogencarbonate and EDTA disodium salt. Tumors were treated with a tumor dissociation kit (Miltenyi Biotec). Afterward, cell suspension was washed in phosphate-buffered saline, centrifuged, and resuspended in a medium consisting of Roswell Park Memorial Institute 1640 Medium (RPMI 1640), fetal calf serum, Minimum Essential Non-Essential Amino Acides (MENEAA), Pen/Strep, L-Glutamin, and sodium pyruvate. The number of viable cells per mL was counted by using 0.4% trypan blue solution (ThermoFisher Scientific) and an automated cell counter (TC20, Bio-Rad Laboratories). In all, 2×10^6 cells per sample were separated for each staining panel. After blocking the cells in a buffer containing mouse serum, fetal calf serum and optional Fc-Block (BD Bioscience), cell surface proteins of interest were labeled with respective antibodies according to manufacturer's instructions. Optionally, cells were subsequently fixed and permeabilized for additional intracellular staining as specified by the manufacturer. The immune cell distribution was measured with a CytoFLEX S flow cytometer (Beckman Coulter) and data were analyzed with the software Cytexpert v2.4 (Beckman Coulter). Panels and analysis are described in the Supplementary material.

Microbiome − sampling, DNA isolation, and sequencing bioinformatic analysis

At the experimental endpoint, gut tissues from all the mice were extracted, fixed and stored at −80°C in DNA/RNA Shield solution (Zymo Research) according to manufacturer's instructions. The samples were processed and analyzed with the Microbiome Analysis Service: Targeted Metagenomic Sequencing (Zymo Research Europe). Details are provided in the Supplementary materials.

Microbiome − bioinformatic analysis

Demultiplexed paired end fastQ reads have been directly downloaded from Zymo Research. Primer sequences (fwd=CCTAYGGGDBGCWGCAG, rev=GACTACNVGGGTMTCTAATCC) have been trimmed off the raw reads via cutadapt (v4.2).[26] Following processing only used forward reads (R1), which were further trimmed to exactly 150 bp from which we called amplicon sequencing variants (ASVs) via Deblur (v1.1.1)[27] through the Qiita platform.[28] ASVs with less than 10 reads in all samples together were dropped. ASVs have been phylogenetically placed into the Greengenes 13.8 99% backbone tree via SEPP (v4.3.10). The resulting tree was used to compute weighted and unweighted UniFrac[29] and Faith's PD alpha diversity.[30] Taxonomy was assigned via Qiime2's "feature-classifier" plugin version 2021.4 against Greengenes 13.8 99% operational taxonomic unit (OTU) sequences.[31] Bacterial features with assigned taxonomy containing the labels c__Chloroplast or f__mitochondria were considered of host or plant origin and removed from the feature table prior to rarefaction. We rarefied the ASV table to 35,000 reads per samples without losing any. The final ASV table comprised 530 ASVs and 42 samples. Sequencing data are available as the public study 15,299 in qiita.ucsd.edu. Microbial analysis notebook is available at https://github.com/jlab/microbiome_Tinganelli_flash.

The following statistical analyses were performed to evaluate the differences between experimental groups: Permutational Multivariate Analysis of Variance (PERMANOVA) with 999 permutations of weighted UniFrac distances (Fig. 5C, D), 2-sided Mann-Whitney on weighted UniFrac (Fig. 5E), PERMANOVA with 999 permutations of unweighted UniFrac distances and 2-sided Mann-Whitney on Bray-Curtis, weighted and unweighted UniFrac distances (Fig. 5F).

Results

In our irradiation setup, we exposed both limbs in the SOBP of the carbon ion beam (Fig. 1). We could therefore access the tissues from both the healthy limb and the one where the tumor was implanted.

UHDR ^{12}C irradiation reduces damage to healthy tissues

To assess the impact of UHDR and CDR ^{12}C exposure on healthy tissues inside the SOBP, we investigated fibrosis formation by collagen deposition using Picrosirius Red staining of the irradiated muscle tissues.[16,32,33] Collagen deposition was significantly lower after the UHDR irradiation. Notably,

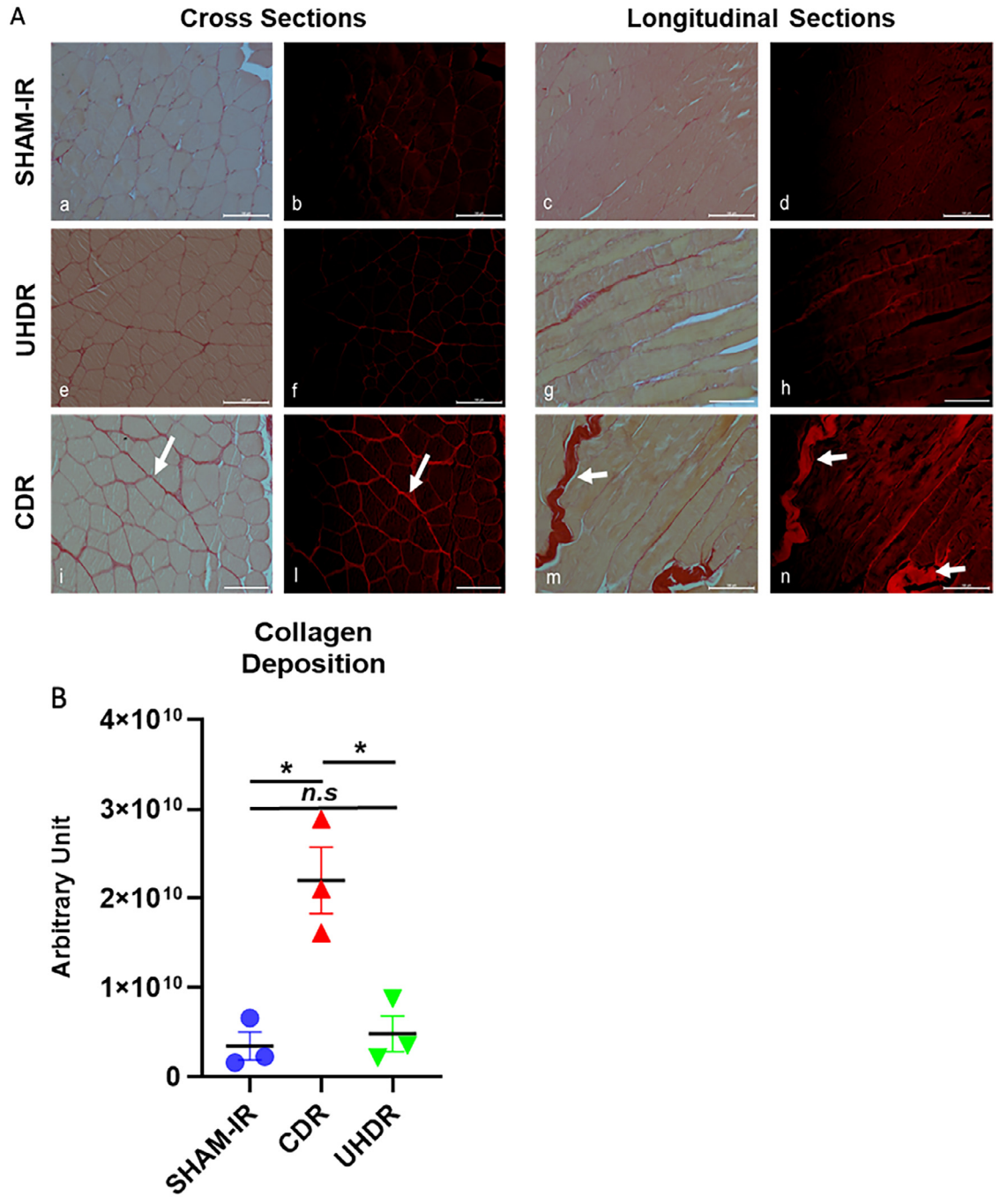

Fig. 2. Muscular damage inside the irradiated healthy limb after UHDR and CDR irradiation. (A) Fibrosis and collagen I deposition were observed in longitudinal and cross-sections of healthy muscle tissue stained with Picrosirius red in sham control (a-d), UHDR-irradiated (e-h), and CDR-irradiated (i-n) mice. The distribution and localization of collagen I in the UHDR-irradiated samples were similar to those in the control mice. A high amount of collagen I was observed between the myofibers (indicated by white arrows) after CDR irradiation. Scale bars: 100 μm. (B) Quantification of collagen I deposition. Blue circles represent sham-irradiated mice (n = 9), red triangles represent CDR-irradiated mice (n = 9), and green triangles represent UHDR-irradiated mice (n = 9). The bars represent the mean values (± standard error of the mean [SEM]). n.s: not significant; *$P < .05$. *Abbreviations:* CDR = conventional dose rate; UHDR = ultra-high dose rate.

the distribution and the localization of Picrosirius Red staining in the FLASH-irradiated muscles closely resembled that of unirradiated muscle tissue, as shown in Figure 2A. The following quantification demonstrated a significant level of collagen I deposition after CDR ^{12}C irradiation compared with UHDR irradiation, as shown in Figure 2B.

UHDR and CDR ^{12}C irradiations lead to equivalent skin toxicity

We further evaluated the skin toxicity in animals irradiated with a dose of 20 Gy in either UHDR or CDR modes. In the UHDR group, 3 out of 14 animals (21%) exhibited no skin damage, whereas the rest had a skin toxicity score of 1. Conversely, in the CDR group, 14 out of 15 animals (93%) displayed a skin toxicity score of 1, and 1 animal (7%) had a skin toxicity score of 2. In all cases, the overall toxicity observed was very low, indicating minimal adverse effects associated with the both irradiation treatments.

UHDR and CDR ^{12}C irradiations lead to equivalent tumor control

The average tumor volume as a function of post-irradiation time is illustrated in Figure 3A. Both UHDR or CDR exposure at 20 Gy led to equivalent tumor control, whereas progressive tumor growth is observed in sham-irradiated animals.

UHDR and CDR ^{12}C irradiations lead to suppression of lung metastases

The LM8 osteosarcoma tumor in the hind limb strongly metastasize in the lung of the mice. We observed a significant decrease in the number of lung metastases in both treatment groups (UHDR: 0.6 ± 0.4; CDR: 2 ± 1) compared with the control group (24 ± 8) (Fig. 3B). We thus confirmed the robust efficacy of CDR in suppressing lung metastases reported in our previous study,[25] and we believe that it can explain the lack of significant differences between the UHDR and CDR modes observed in the present work.

UHDR ^{12}C irradiation does not differentially impact on local and systemic anti-tumor immune responses 28 days after exposure

To investigate the effects of UHDR ^{12}C irradiation on the local immune response in the tumors, we analyzed the number of cells stained positive for CD8, a marker for cytotoxic T-cells, 28 days after exposure. Both UHDR and CDR ^{12}C led to a significant increase in CD8-positive cells compared with the controls (Fig. 4A). This indicates increased infiltration of cytotoxic T-cells upon irradiation. However, no significant differences in the number of CD8-positive cells were found between UHDR and CDR, suggesting no increased efficiency of UHDR ^{12}C with respect to a local radiation-induced anti-tumor immune response at 28 days after the treatment.

Next, to examine whether UHDR and CDR differentially impact the potential to induce systemic immune responses

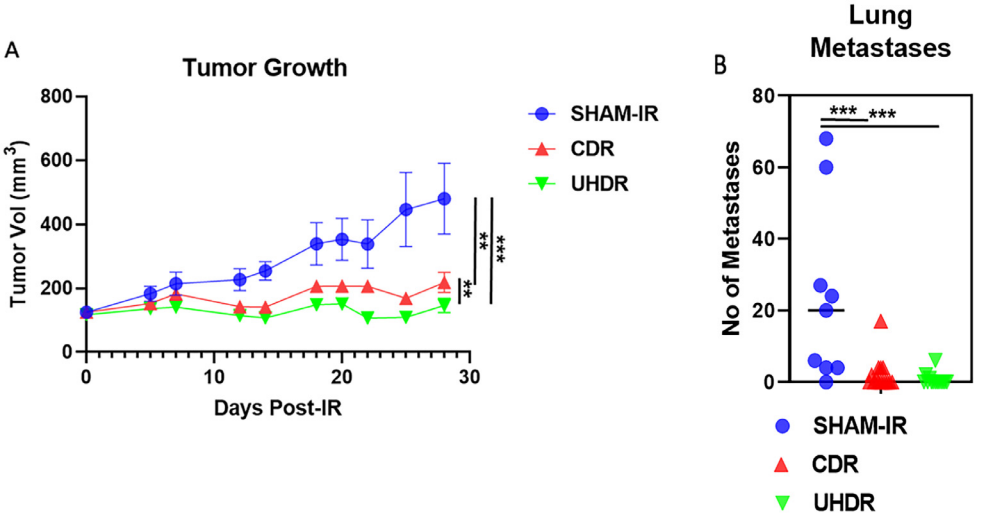

Fig. 3. Comparative analysis of tumor volume reduction and metastatic nodule reduction after CDR and UHDR irradiation. (A) The reduction of tumor volume is presented over a span of 28 days post-irradiation. Blue circles represent sham-irradiated mice (n = 10), red triangles represent CDR-irradiated mice (n = 15), and green triangles represent UHDR-irradiated mice (n = 14). Black bars indicate mean values ± SEM for each treatment group. (B) The reduction in the number of metastatic nodules after CDR and UHDR irradiation is shown. Similar to Figure 2, blue circles represent sham-irradiated mice (n = 10), red triangles represent CDR-irradiated mice (n = 15), and green triangles represent UHDR-irradiated mice (n = 14). Black bars also indicate mean values ± SEM for each treatment group. $^{**}P < .005$; $^{***}P < .001$. *Abbreviations:* CDR = conventional dose rate; SEM = standard error of the mean; UHDR = ultra-high dose rate.

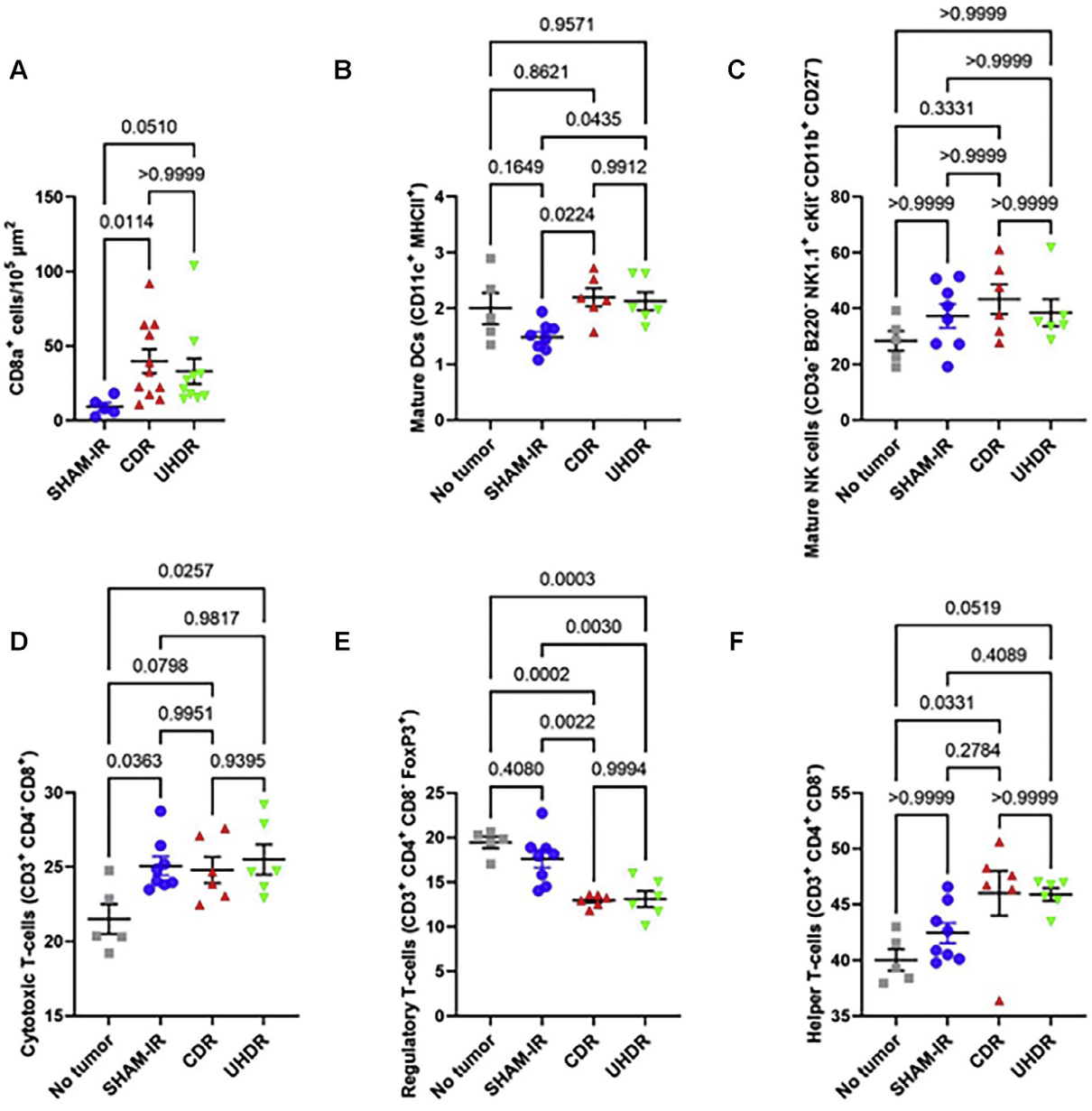

Fig. 4. Infiltration of $CD8a^+$ cells in tumors and splenic immune cell populations 28 days after CDR or UHDR treatment. (A) Numbers of $CD8a^+$ cells were normalized to an area of 10^5 μm^2 for each analyzed tumor; black bars indicate mean values ± SEM for each treatment group; SHAM-IR n = 5, CDR n = 11, UHDR n = 10. (B-F) Percentages of splenic immune cell populations; no tumor n = 5, SHAM-IR n = 8, CDR n = 6, UHDR n = 6. Black bars indicate mean values ± SEM for each treatment group for B: mature dendritic cells, C: mature NK cells, D: cytotoxic T-cells, E: regulatory T-cells and F: helper T-cells. The *P* values (Kruskal-Wallis test) are indicated individually. *Abbreviations:* CDR = conventional dose rate; NK = natural killer; SEM = standard error of the mean; UHDR = ultra-high dose rate.

with putative effects on metastases, we analyzed immune cell populations in the spleen and lymph nodes. We screened for dendritic cells, B-cells, natural killer (NK) cells in spleen, and several subpopulations of T-cells in spleen and lymph nodes. Analyses of the main populations of immune cells in spleen and lymph nodes revealed no significant changes (Figs. E1 and E2A). By tendency, however, sham-irradiated tumor-bearing mice showed slight differences in the percentage of immune cells compared with no-tumor mice, which were partly reversed by both irradiation modes. The only significant radiation-induced increase was found in splenic NK cells after CDR exposure (Fig. E1C).

The amount of splenic mature dendritic cells (CD11c+ MHCII+ cells, Fig. 4B) was found to be significantly ($P < .05$) increased after exposure to both radiation modes, CDR, and UHDR, compared with sham-irradiated tumor-bearing mice, but no differences between the modes occurred. In contrast, the percentage of mature NK cells (CD3− CD19− CD11b+ CD27− cKit− NK1.1+ cells, Fig. 4C) did not reveal any significant differences but, again, showed a tendency to

increase in tumor-bearing mice (both irradiated and sham-irradiated). This was the same for cytotoxic T-cells (CD3+ CD8+ CD4−) but the change differed significantly from no-tumor mice (Fig. 4D). Radiation-induced changes, both compared with healthy and sham-irradiated mice, were found for regulatory T-cells (CD3+ CD4+ CD8− FoxP3+) and helper T-cells (CD3+ CD8− CD4+) (Fig. 4E and 4F). Although the number of regulatory T-cells significantly decreased compared with both controls (Fig. 4E), the amount of helper T-cells increased, however, significantly only when CDR was compared with no-tumor mice (Fig. 4F). Yet again, no significant differences between the 2 modes, CDR and UHDR, were found. When the respective T-cell subpopulations were analyzed in lymph nodes, no differences were found for cytotoxic T-cells and helper T-cells (Fig. E2B, C) but the results for regulatory T-cells stemming from spleen were confirmed by tendency (Fig. E3D).

UHDR and CDR ^{12}C irradiations push the microbiome back toward the healthy state

Taxonomic composition of the gut microbiome (Fig. 5A) and pairwise beta-diversity distances (Fig. 5B) was assessed via 16S rRNA profiling. The presence of limb osteosarcoma modifies the gut microbiome in mice, as indicated by statistically significant differences between the no-tumor mice and tumor-bearing, sham-irradiated mice (Fig. 5C). The 8 untreated mice had a significantly different gut microbiome from the irradiated tumor-bearing mice (Fig. 5D). The gut microbiome of the irradiated mice resembled that of the healthy mice significantly closer than the microbiome of the sham-irradiated animals for both treatment regimens (Fig. 5E, $P < 10^{-7}$). We detect significant difference between UHDR and CDR treatments (Fig. 5F); however, it did not lead to significantly closer microbiomes compared with the healthy mice.

Discussion

We report here the first experiment on the FLASH effect in an animal model irradiated in the SOBP of a heavy ions beam. Our objective was to determine whether FLASH irradiation in the Bragg-peak region elicits distinct biological effects compared with low-LET irradiation, particularly concerning immune response stimulation, reduction of lung

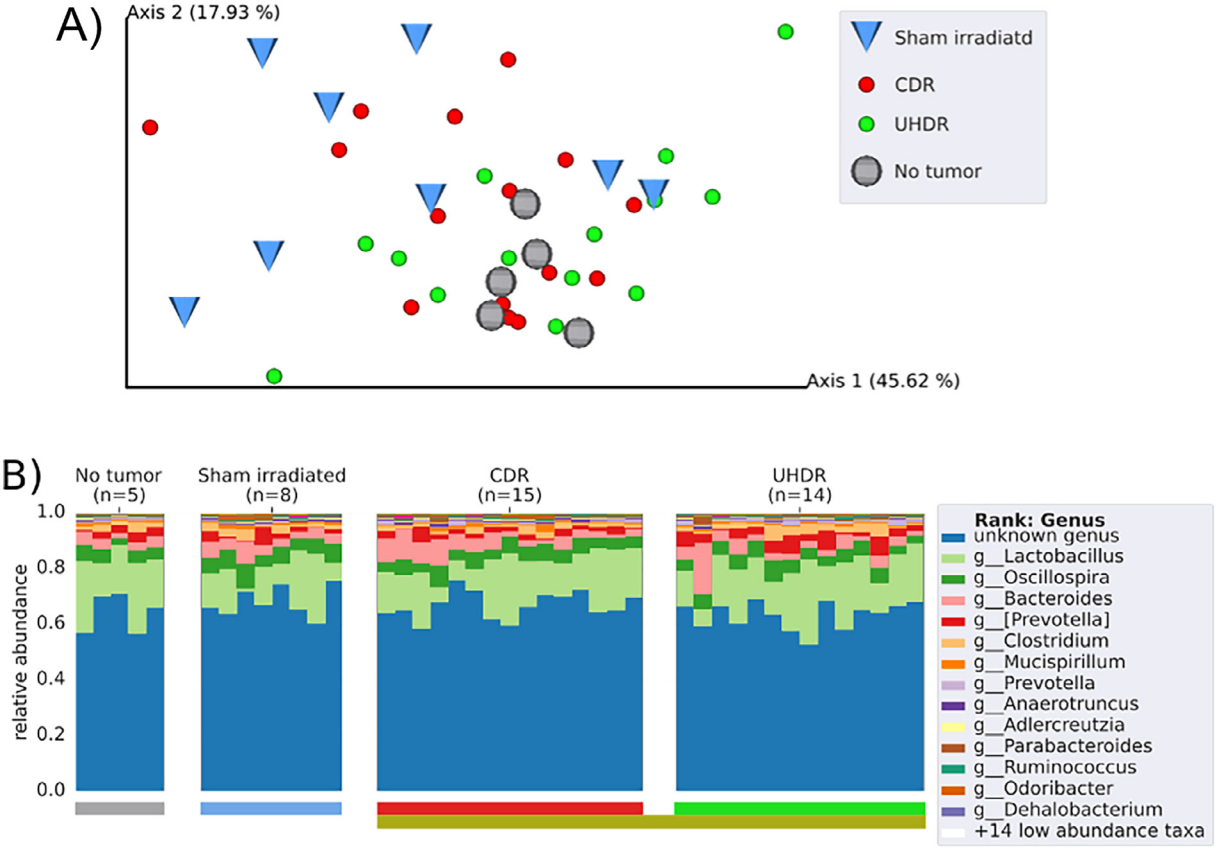

Fig. 5. Changes in the gut microbiome caused by the presence of tumor and by different irradiation modes. (A) PCoA ordination of pairwise unweighted UniFrac distances. (B) Taxonomy bar plot on genus rank. (C,D,F) Visualizations of PERMANOVA tests that consider differences within group (left and right box) and across group (white box in the middle). (E) Distances from UHDR, CDR to control, (no tumor) group (gray) and to sham irradiated tumor-bearing mice (blue). Distances are compositional, ie, low distance to gray implies high distance to sham and vice versa. *Abbreviations:* CDR = conventional dose rate; PCoA = principal coordinates analysis; PERMANOVA = permutational multivariate analysis of variance; UHDR = ultra-high dose rate.

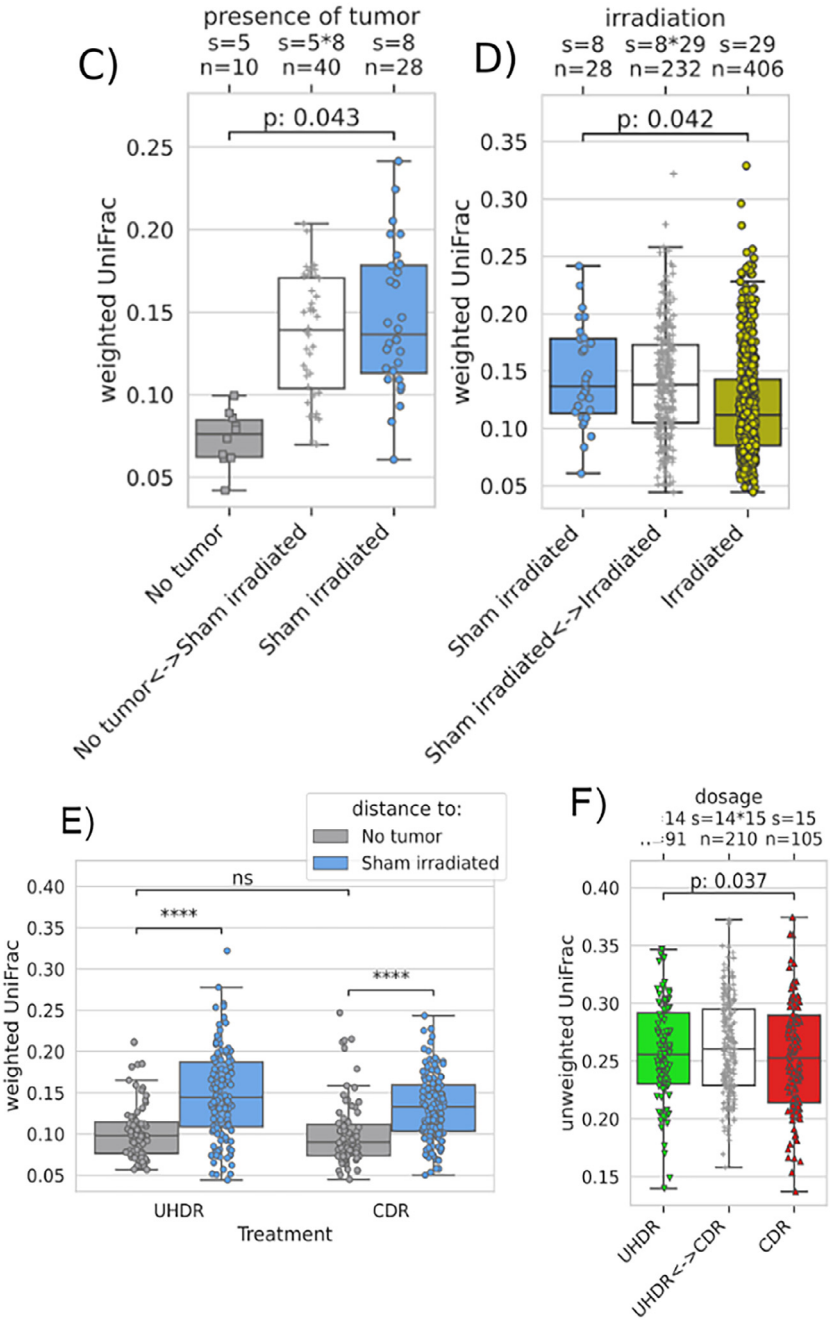

Fig. 5. Continued.

metastases, and alterations in the mouse gut microbiome. We observed that animals irradiated at CDR within the ^{12}C SOBP had increased collagen deposition, a hallmark of radiation-induced fibrosis in the healthy muscle tissues. In contrast, those irradiated at UHDR had collagen levels similar to those in nonirradiated control animals. We also investigate limb atrophy or skin damage after radiation. However, a dose of 20 Gy did not cause any atrophy of the paw in either treatment. Regarding skin damage, we found a very low toxicity even in the conventional irradiated animals, showing no significant differences between the 2 treatment modalities. Most animals of both treatments developed skin damage with a score of 1, characterized by redness and slight desquamation, as detailed in Table 1.

This confirms the sparing effect of UHDR radiation, even with high-LET ^{12}C beams. This result is valued for testing the current mechanistic models of the FLASH effect, which generally predict a decrease of the effect at high-LET.[11] High-LET radiation is indeed expected to diminish the FLASH effect for 2 main reasons. First, high-LET ions are less affected by the oxygen levels in the irradiated tissues, which reduces the oxygen enhancement ratio. Second, at high LET, achieving oxygen depletion would necessitate significantly higher doses. This is because denser ionization

Table 1 Total and relative (in brackets) numbers of animals exhibiting skin damage in Control, sham-irradiated (SHAM-IR), ultra-high dose rate (UHDR), and conventional dose rate (CDR) experimental groups

Grade	Description	Control	SHAM-IR	UHDR	CDR
0	No damage	5 (100%)	10 (100%)	3 (21%)	
1	Skin peeling and redness			11 (79%)	14 (93%)
2	Small wounds				1 (7%)

tracks promote intratrack recombination of radicals, which inhibits the usual oxygen-consuming processes.[11]

Similar to our previous low-LET C-ions[16] we found no significant differences between the CDR and UHDR groups in tumor control. The measurements of tumor sizes showed that the UHDR-irradiated tumors were slightly smaller than those irradiated at CDR. This size reduction could potentially be attributed to the inflammation in the healthy tissues surrounding the tumor, caused by CDR but not UHDR irradiation.

In our previous work,[16] we observed a decrease in the occurrence of lung metastases after ^{12}C UHDR irradiation. In the SOBP, both CDR and UHDR exhibited equal efficacy in suppressing the lung metastasis formation. The ability of high-LET ^{12}C ions to significantly inhibit metastatic development at CDR has already been demonstrated in our earlier.[25] Looking at the generalized immune response, both UHDR and CDR irradiations led to a significant increase of infiltrated CD8+ cytotoxic T-cells in the tumor and a decrease of Treg cells, but no significant differences were observed between CDR and FLASH. Taken together, these data suggest that SOBP (high-LET) C-ions elicit a strong immune response, and UHDR conditions do not modify it.

The impact of different radiation strategies on the microbiome is an area of ongoing research and investigation. Some preliminary research has suggested that radiation therapy, especially when administered at high doses (which are indeed a requirement for the FLASH effect), may lead to alterations in the gut microbiome.[33]

To assess potentially detrimental effects of the irradiation on the gut microbiome of mice, we profiled their bacterial colon content via 16S rRNA amplicon sequencing. Our results suggest that tumors negatively affect the gut microbiome. However, when treated with irradiation, regardless of the dose rate, this shift can be partially reversed. Both treatments tend to guide the microbiome back to a healthier state.

In conclusion, our results show that normal tissue sparing and tumor control are maintained when high-LET heavy ions are used at UHDR in a murine osteosarcoma model. On the other hand, the immune response and alterations in the gut microbiome were induced by SOBP C-ions but were not dependent on dose rate. These results are relevant for understanding the mechanisms of the FLASH effect, because all the present models are ostensibly affected by the radiation LET. Along with our previous results in plateau-phase C-ions,[16] they demonstrate the feasibility of UHDR C-ion radiation therapy.

Nonetheless, it is important to note that one of the limitations of this study lies in the use of a single animal model and tumor type. The results presented here, although valuable for understanding the potential of FLASH with high-LET carbon ions, cannot be broadly generalized. Future experiments using additional animal models and tumor types are necessary to conclusively confirm the efficacy and understand the mechanisms of the FLASH effect with carbon ions.

References

1. Vozenin MC, Bourhis J, Durante M. Towards clinical translation of FLASH radiotherapy. *Nat Rev Clin Oncol* 2022;19:791-803.
2. Favaudon V, Caplier L, Monceau V, et al. Ultrahigh dose-rate FLASH irradiation increases the differential response between normal and tumor tissue in mice. *Sci Transl Med* 2014;6:245ra93.
3. Wilson JD, Hammond EM, Higgins GS, Petersson K. Ultra-high dose rate (FLASH) radiotherapy: silver bullet or fool's gold? *Front Oncol* 2020;9:1563.
4. Montay-Gruel P, Acharya MM, Petersson K, et al. Long-term neurocognitive benefits of FLASH radiotherapy driven by reduced reactive oxygen species. *Proc Natl Acad Sci USA* 2019;116:10943-10951.
5. Favaudon V, Labarbe R, Limoli CL. Model studies of the role of oxygen in the FLASH effect. *Med Phys* 2022;49:2068-2081.
6. Labarbe R, Hotoiu L, Barbier J, Favaudon V. A physicochemical model of reaction kinetics supports peroxyl radical recombination as the main determinant of the FLASH effect. *Radiother Oncol* 2020;153:303-310.
7. Abolfath R, Grosshans D, Mohan R. Oxygen depletion in FLASH ultra-high-dose-rate radiotherapy: a molecular dynamics simulation. *Med Phys* 2020;47:6551-6561.
8. Jin JY, Gu A, Wang W, et al. Ultra-high dose rate effect on circulating immune cells: a potential mechanism for FLASH effect? *Radiother Oncol* 2020;149:55-62.
9. Shi X, Yang Y, Zhang W, et al. FLASH X-ray spares intestinal crypts from pyroptosis initiated by cGAS-STING activation upon radioimmunotherapy. *Proc Natl Acad Sci USA* 2022;119:e2208506119.
10. Song CW, Terezakis S, Park W-Y, et al. Preferential tumor vascular damage is the common antitumor mechanism of high-dose hypofractionated radiation therapy: SABR, spatially fractionated radiation therapy, and FLASH radiation therapy. *Int J Radiat Oncol Biol Phys* 2023;117:701-704.
11. Weber UA, Scifoni E, Durante M. FLASH radiotherapy with carbon ion beams. *Med Phys* 2022;49:1974-1992.
12. Durante M, Debus J, Loeffler JS. Physics and biomedical challenges of cancer therapy with accelerated heavy ions. *Nat Rev Phys* 2021;3:777-790.
13. Castro JR, Kirkby NF, Burnet NG, et al. Treatment of cancer with heavy charged particles. *Int J Radiat Oncol Biol Phys* 1982;8:2191-2198.
14. Tobias CA. Failla Memorial lecture. The future of heavy-ion science in biology and medicine. *Radiat Res* 1985;103:1-33.
15. Tinganelli W, Sokol O, Quartieri M, et al. Ultra-high dose rate (FLASH) carbon ion irradiation: Dosimetry and first cell experiments. *Int J Radiat Oncol Biol Phys* 2022;112:1012-1022.
16. Tinganelli W, Weber U, Puspitasari A, et al. FLASH with carbon ions: Tumor control, normal tissue sparing, and distal metastasis in a mouse osteosarcoma model. *Radiother Oncol* 2022;175:185-190.

17. Tinganelli W, Durante M. Carbon ion radiobiology. *Cancers (Basel)* 2020;12:3022.
18. Sokol O, Durante M. Carbon ions for hypoxic tumors: are we making the most of them? *Cancers (Basel)* 2023;15:4494.
19. Luoni F, Weber U, Boscolo D, et al. Beam monitor calibration for radiobiological experiments with scanned high energy heavy ion beams at FAIR. *Front Phys* 2020;8:1-11.
20. Simenov Y, Weber U, Schuy C, et al. Monte Carlo simulations and dose measurements of 2D range-modulators for scanned particle therapy. *Z Med Phys* 2021;31:203-214.
21. Wegner KA, Keikhosravi A, Eliceiri KW, Vezina CM. Fluorescence of picrosirius red multiplexed with immunohistochemistry for the quantitative assessment of collagen in tissue sections. *J Histochem Cytochem* 2017;65:479-490.
22. López De Padilla CM, Coenen MJ, Tovar A, et al. Picrosirius red staining: revisiting its application to the qualitative and quantitative assessment of collagen Type I and Type III in Tendon. *J Histochem Cytochem* 2021;69:633-643.
23. Charuchinda W, Horst F, Simeonov, et al., et al. 3D range-modulators for proton therapy: Near field simulations with FLUKA and comparison with film measurements. *J Phys Conf Ser* 2023;2431:012081.
24. Weber U, Kraft G. Design and construction of a ripple filter for a smoothed depth dose distribution in conformal particle therapy. *Phys Med Biol* 1999;44:2765-2775.
25. Helm A, Tinganelli W, Simoniello P, et al. Reduction of lung metastases in a mouse osteosarcoma model treated with carbon ions and immune checkpoint inhibitors. *Int J Radiat Oncol Biol Phys* 2021;109:594-602.
26. Martin M. Cutadapt removes adapter sequences from high-throughput sequencing reads. *EMBnet J* 2011;17:10-12.
27. Amir A, McDonald D, Navas-Molina JA, et al. Deblur rapidly resolves single-nucleotide community sequence patterns. *Am Soc Microbiol* 2017;2:1-7.
28. Gonzalez A, Navas-Molina JA, Kosciolek T, et al. Qiita: rapid, web-enabled microbiome meta-analysis. *Nat Methods* 2018;15:796-798.
29. Lozupone C, Knight R. UniFrac: a new phylogenetic method for comparing microbial communities. *Appl Environ Microbiol* 2005;71:8228-8235.
30. Faith DP. Conservation evaluation and phylogenetic diversity. *Biol Conserv* 1992;61:1-10.
31. Bolyen E, Rideout JR, Dillon MR, et al. Reproducible, interactive, scalable and extensible microbiome data science using QIIME 2. *Nat Biotechnol* 2019;37:852-857.
32. James J, Bosch KS, Aronson DC, et al. Sirius red histophotometry and spectrophotometry of sections in the assessment of the collagen content of liver tissue and its application in growing rat liver. *Liver* 1990;10:1-5.
33. Simoniello P, Wiedemann J, Zink J, et al. Exposure to carbon ions triggers proinflammatory signals and changes in homeostasis and epidermal tissue organization to a similar extent as photons. *Front Oncol* 2016;5 294.